



Transporting cold atoms using an optically compensated zoom lens

Jae Hoon Lee ¹, Haejun Jung,² Jae-yoon Choi ², and Jongchul Mun^{1,*}

¹*Korea Research Institute of Standards and Science, Daejeon 34113, Republic of Korea*

²*Department of Physics, Korea Advanced Institute of Science and Technology, Daejeon 34141, Republic of Korea*



(Received 5 June 2020; revised 3 November 2020; accepted 5 November 2020; published 10 December 2020)

We report the design and application of an optically compensated zoom lens supporting a moving optical dipole trap for transporting cold atoms. The proposed zoom lens is designed to have tunable magnification in a compact form factor which can significantly reduce the required long optical path lengths in conventional moving optical dipole trap systems. Without the need of mechanical cams for zooming, the optically compensated zoom lens has the ability to control the position of the trap along the optical axis with high precision while maintaining a constant trap depth by conserving the numerical aperture of the laser beam focus during the transport. We experimentally comprise an optically compensated zoom lens having dimensions of $\lesssim 20$ cm in length, which can be readily configured to suit a wide range of desired transport lengths from 0.15 to 3 m and displacement magnifications from 7 to 100. The performance of our moving optical dipole trap is tested for a target transport length of 600 mm using a 532 nm laser beam on laser-cooled ytterbium atoms. The atoms can be transported to an adjacent vacuum chamber using this optically compensated zoom lens with $\sim 89\%$ efficiency.

DOI: [10.1103/PhysRevA.102.063106](https://doi.org/10.1103/PhysRevA.102.063106)

I. INTRODUCTION

Experiments using cold neutral atoms have been extensively developed and continuously improved for decades in the pursuit of efficient cooling of the atomic motion accompanied by precise control and measurement of its quantum state [1–6]. At present, cutting edge apparatus for these experiments now require optical and electronic systems that are considerably complex with densely packed elements such as high-resolution microscopes [7,8], optical cavities [9,10], blackbody radiation shields [11], and high-field magnetic coils [12]. As of late, some noteworthy hybrid quantum experiments require cold neutral atoms to be coupled to trapped ions [13] or nanophotonic devices [14–17] in order to probe quantum systems in formerly unexplored regimes. Keeping in mind that cold atom production fundamentally demands an ultrahigh-vacuum (UHV) environment, these experimental components are more often than not incompatible in a single vacuum chamber.

The most prominent way of overcoming these experimental restrictions is to transport the cold atomic sample from where it was prepared to a neighboring position with better accessibility and preferably improved isolation from the environment. Several methods for transporting cold atoms have been developed such as the optical lattice conveyor belt [18,19], transversely dynamic optical tweezer [20–22], velocity selective cooling [23], magnetic trap transport [24–29], and axially moving optical dipole trap (ODT) [30–32]. The former three techniques are typically limited to atom displacement of short distances within a single UHV chamber due to technical impracticalities or transfer in-

efficiencies. In the case where well controlled transfer of cold atoms into a separate UHV chamber is necessary, procedures employing a moving magnetic trap or optical dipole trap is generally adopted.

Implementing magnetic traps for atom transport over large distances involve either a moving magnetic coil [24,25] or a stationary array of magnetic coils that are installed as close as possible around the UHV system [27,28]. It is common for the coils to require water cooling as high current is usually applied to hold the atoms against gravity. These intrusive experimental conditions make it difficult to apply magnetic coils for transport in many experiments. Moreover, working with high magnetic fields can be detrimental for various precision measurement experiments due to the induced eddy currents and gradual magnetization of the surrounding components [33]. In contrast to magnetic traps, ODTs use focused laser beams to trap atoms via optical dipole force. Implementation of focused optical traps is currently used broadly throughout the scientific community for trapping and manipulation of nano- and biomaterials [34–39]. In cold atom experiments such as that in this study, optical access to the atoms is obtained through UHV viewport windows which happen to be relatively copious in laser-cooling setups. High-power lasers at far-detuned wavelengths are regularly used for ODTs in order to suppress photon scattering and increase the atom trapping lifetime [40]. Comparatively, an ODT is straightforward to implement as long as proper optical components with high damage thresholds are used.

Moving the ODT for atom transport can be accomplished through various schemes. Mounting a focusing lens on an air-bearing stage in conjunction with a conjugate or afocal imaging setup is a widely used reliable method [41]. Unfortunately, the air-bearing stages used for these setups are fairly expensive and the optical path needed to shape the

*jcmun@kriss.re.kr

input beam, travel the length of the stage while creating an intermediate focus, and image the intermediate focus on the targeted atom position is onerously long for some setups. Recently, focus-tunable polymer lenses have been successfully used to displace ODTs for atom transport [42]. Although these systems can be extremely compact with exceedingly fast response times, the clear aperture sizes are very limited compared to regular glass lenses, and their focal lengths need to be compensated for due to thermal affects which should be monitored in a circumspect manner.

Here we design and experimentally implement an optically compensated zoom (OCZ) lens [43–45] to transport cold ^{174}Yb atoms by shifting the position of an ODT. Zoom lenses are typically designed to change the effective focal length while keeping the image plane position constant. However, in this study a zoom lens is used to move the focal point along the optical axis via insertion of a collimated laser beam. Utilizing an OCZ lens where the zoom is controlled by a programmable translation stage has many advantages. First, the OCZ lens magnifies small displacements of the translation stage for large movements of the ODT position without requiring an intermediate focus. Consequently, the OCZ lens drastically reduces the overall form factor of the optical setup compared to previous translation stage based ODT systems offering a new technique toward system miniaturization. Second, the OCZ lens is highly customizable since the distance between the lenses can be continuously tuned for a precisely configured result. The vast choice of off-the-shelf lenses along with the option to purchase custom manufactured lenses for the lens assembly further expands the customizability of the OCZ lens. Third, the compensating design of the OCZ lens conserves the numerical aperture (NA) as the focus is shifted, providing a constant trap depth of the ODT during travel. Fourth, unlike a mechanically compensated zoom lens, the OCZ lens does not require nonlinear relative motion between the comprising lenses for zoom. Therefore precise control of the zoom can be obtained by mounting the moving components on a linear translation stage providing high precision, stability, and simplicity. Finally, due to the fact that customary glass lenses are used, there is much potential for adding more complexity to the design, e.g., an achromatic ODT for dual species transport or a precisely calibrated position-dependent beam waist for efficient cooling during transport.

II. OPTICALLY COMPENSATED ZOOM LENS DESIGN

The five element OCZ lens that we incorporate consists of two groups of lenses. Three positive lenses (L_1, L_3, L_5) comprise group A while group B contains two negative lenses (L_2, L_4), as shown in Fig. 1(a). Lenses from the two groups are placed alternately such that the spacings between the three positive lenses, and the spacing between the two negative lenses are identical and fixed for a given configuration. Therefore, the composite zoom lens can be described as being comprised of two element groups where the effective focal length of the composite optical system can be changed by moving the two lens groups relative to each other along the optical axis. The relative position between the lens groups is defined by the displacement parameter x depicted in Fig. 1(a). In this study, we implement a symmetrical lens layout where

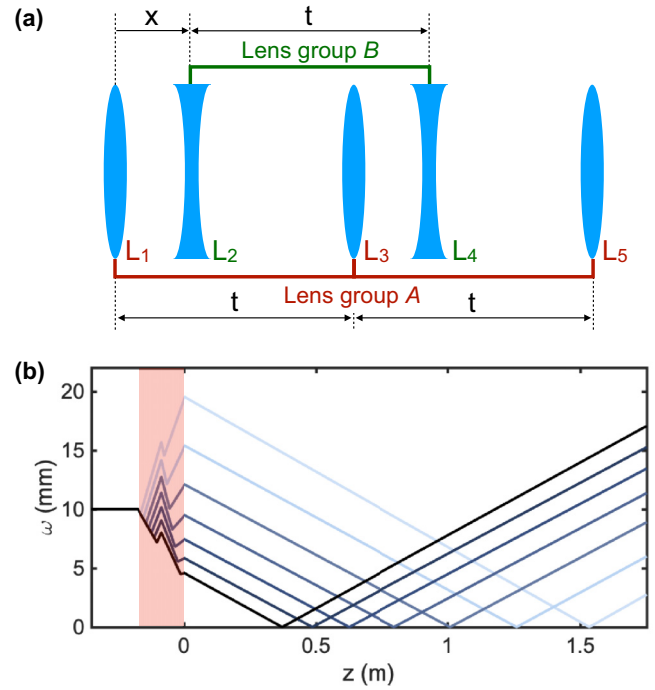


FIG. 1. (a) Schematic of the five element OCZ lens comprised of lens group A (stationary) and lens group B (movable). The length t is a main parameter for the configuration, and the position x actuates the zoom. (b) Calculation of the $1/e^2$ beam radius $w(z)$ along the optical axis z , when a collimated Gaussian beam of initial width 10 mm propagates into the OCZ lens. The last element of the OCZ lens L_5 is designated to be at $z = 0$. The red-shaded region $-172.8 \text{ mm} < z < 0$ indicates where the OCZ lens is located. The seven plots correspond to $w(z)$ for equidistant zoom positions from $x = 10 \text{ mm}$ to $x = 70 \text{ mm}$, which are colored progressively from light to dark blue. See the main text for specific lens parameters.

L_1 and L_5 have identical focal lengths as do L_2 and L_4 . The reasoning for choosing this type of configuration will be explained in the next section.

An OCZ lens is advantageous compared to a mechanically compensated zoom lens since nonlinear and independent lens motion of each optical element is not required for zooming. Although mechanically compensated zoom lenses are predominantly used for commercial zoom lenses today, it proves to be difficult to employ for applications requiring ultraprecise zoom control with high stability and accuracy of the effective focal length. These deficiencies of mechanically compensated zoom lenses originate primarily from its use of mechanical cams for nonlinear relative movement of the optical elements. Moving ODTs for cold atoms require accurate positioning of the focal point in order to efficiently load the ODT with cooled atoms and deliver them to their exact destinations. The movement of the focal position must also be precisely controlled to minimize the loss of trapped atoms due to excessive acceleration during transport and parametric heating from unwanted fluctuation of the trap position. Considering these requirements for a moving ODT, we insert a collimated Gaussian beam into an OCZ lens where the effective back focal length, i.e., the ODT position, is precisely tuned by

controlling the displacement of lens group B , namely, the zoom.

A. Gaussian beam calculations

Figure 1(b) illustrates how a Gaussian beam propagates through the OCZ lens for various focal lengths adjusted with the zoom. The $1/e^2$ radius of the Gaussian beam w is plotted against the optical axis z centered at L_5 . Calculations of the Gaussian beam intensity profiles were done to first order for seven different zoom focal lengths determined by x . We assume that the OCZ lens consists of five thin lenses with infinite aperture sizes and focal lengths of $[f_1, f_2, f_3, f_4, f_5] = [250, -80, 80, -80, 250]$ mm. The intragroup lens spacing for this calculation was set to $t = 86.4$ mm corresponding to the actual parameter used in our experiment. A collimated Gaussian beam of radius $w = 10$ mm and wavelength $\lambda = 532$ nm enters the OCZ lens and subsequently exits in a focusing manner. The Gaussian beam is focused at variable positions depending on the zoom which is set by x . Note that this is strictly a first-order calculation to provide basic understanding of the OCZ lens under zooming motion in the absence of any higher-order effects due to aberration and distortion. These ideal calculations contribute important insight when configuring the OCZ lens to given specifications such as the effective focal length, numerical aperture, Rayleigh range (z_R), and optimal stop locations.

Linear motion of the lens group B by ~ 70 mm leads to the effective focal length changing by more than 1.2 m for this configuration of $t = 86.4$ mm. The working distance z_{WD} , defined by the distance along the optical axis from L_5 to the focus position, monotonically decreases as x is increased. By observing the incoming and outgoing angles of the beam edge in the far-field regime, i.e., $\Theta = 2 \arctan [dw(z)/dz]$ when $|z - z_{WD}| \gg z_R$, we can deduce that the beam divergence is conserved throughout the zooming range. This observation infers that the beam waist radius w_0 will be kept constant during the zooming motion by virtue of the inherent compensating capabilities of the OCZ lens. Furthermore, beam propagation within the OCZ lens [red-shaded region in Fig. 1(b)] shows that the beam size is largest at L_3 for $x > 25$ mm, and at L_5 otherwise. This behavior should be taken into account when selecting lens diameters, and a proper aperture stop should be provided to prevent inconsistent beam waist characteristics due to varying aperture limitations during zoom motion.

Calculations of the numerical aperture for given working distances is plotted in Fig. 2(a). The parameters of the OCZ lens configuration that are used for this calculation are the same as those in Fig. 1(b). The range of working distances shown in Fig. 2 corresponds to zoom positions from $x = 20$ mm to $x = 63$ mm. The calculations show that as the focus is moved along the optical axis by a distance of 800 mm the numerical aperture is maintained to within 2.5% of the mean value 0.0120. Naturally, as we increase the input Gaussian beam width the numerical aperture will increase proportionally resulting in a smaller beam waist. The deviating profile of the numerical aperture across the working distances will simply scale with the input beam size. Note that the small deviations of the numerical aperture shown here arise from solely first-order calculations, and any additional higher-order

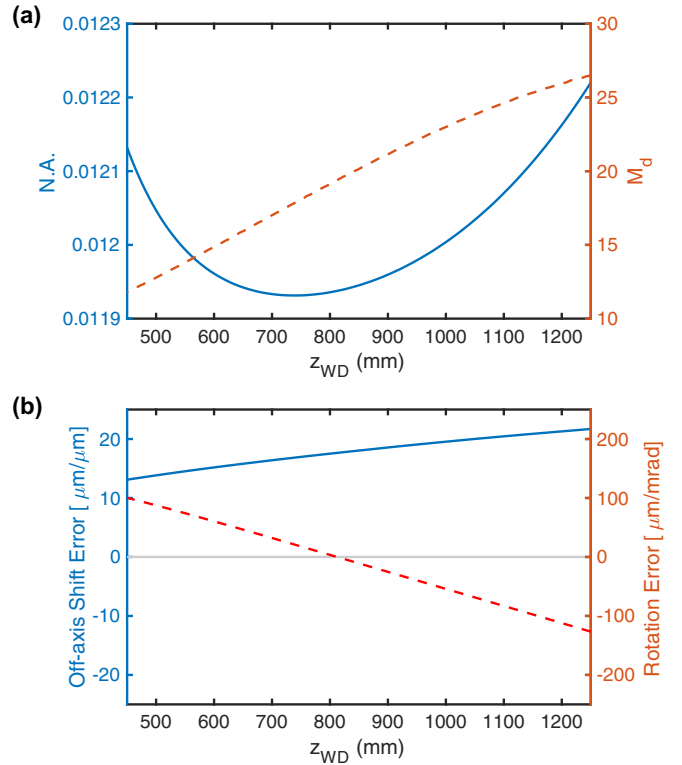


FIG. 2. (a) Calculated numerical aperture (solid line) and the displacement magnification M_d (dashed line) as a function of the working distance. The input beam size is 10 mm and $t = 86.4$ mm. (b) Off-axis shift error (solid line) and rotation error (dashed line) are also calculated for the same range of working distance.

effects or alignment imperfections will further modify the compensating characteristics of the zoom lens.

We define a quantity that describes the amount of zoom motion needed to move the focal point a given distance which we label as displacement magnification $M_d = -dz_{WD}/dx$. As the working distance does not change linearly with the zoom position, M_d is not constant relative to z_{WD} . In Fig. 2(a) we plot M_d values with respect to the working distance for the zoom lens configuration $t = 86.4$ mm. This curve implies that when lens group B moves along the direction decreasing x at a constant speed, the focal point will slightly accelerate as it advances further away from L_5 . In the case where the speed of the focal point $v_{ODT} = dz_{WD}/dt$ must be kept constant, one may control the speed of the zoom motion $v_x = dx/dt$ to compensate for the change in $M_d(x)$.

We also study the effect of lateral lens alignment errors while zooming which are shown in Fig. 2(b) calculated using the beam propagation method. We assume thin lenses and overall ideal conditions except for the small lateral alignment errors of interest that are prone to mechanical vibrations during zoom motion. We consider the case in which the lenses in group A are perfectly aligned while group B exhibits off-axis shift and rotation errors with respect to the optical axis. The off-axis shift error refers to the amount of lateral translation the focal point experiences when the two lenses in group B shift by the same amount in the transverse direction. Calculations show that the focal point shifts off axis by $\sim 18 \mu\text{m}$

on average when lens group B is shifted off axis by $1\ \mu\text{m}$. The exact amount of shift depends on the zoom position and increases with the working distance.

The rotation error shown in Fig. 2(b) ascribes to a situation when the focal point drifts off the optical axis due to lens group B rotating about an axis which is located at midpoint between the two lenses and directed perpendicular to the optical axis. This rotational error is plotted as the focal point lateral displacement per rotation angle. Since for rotations the two lenses of group B move in opposite directions and thus shift the focal point in a canceling manner, the total shift of the focal point is greatly suppressed for the rotational error compared with the off-axis shift error. For a rotation corresponding to a $1\ \mu\text{m}$ shift in lens alignment, the focal point shifts off axis by $< 2\ \mu\text{m}$. Therefore, the rotation error can be described as being more than an order of magnitude smaller than the off-axis shift error throughout most of the zoom range. Note that the absolute amount of lateral displacement of the ODT from the optical axis is not an issue for atom loading and transporting as long as higher-order effects such as aberration do not substantially degrade the intensity profile of the focus. The calculations of Fig. 2(b) are imperative for quantifying position fluctuations of the ODT, which can induce parametric heating of the trapped atoms, as a consequence of mechanical vibrations transmitted to the lenses from the linear translation stage amid zoom motion. The calculations suggest that in-phase lateral vibrations of L_2 and L_4 should be of concern, much more than those out of phase, when designing the mechanical mount for lens group B . These results also provide information for quantitatively evaluating whether a linear stage has sufficient straightness and flatness performance to adequately actuate the zoom.

B. Configuring the optically compensated zoom lens

The focal lengths of the five lenses comprising the OCZ lens in this article was chosen bearing in mind a target z_{WD} range of $\sim 500\ \text{mm}$ to $\sim 1500\ \text{mm}$ via zoom while using only commercial off-the-shelf lenses. Starting from an analytic approach [43], we numerically found the set of focal lengths that produced satisfying outcomes under the limited choice of lenses that are commercially available. Determining the optimal set of lenses to use is a convoluted process since most of the parameters are intertwined for a wide range of optimization targets which are in turn also correlated and need to be adequately compromised for well-rounded performance. Nevertheless, we provide a hand-waving qualitative argument for how to choose the focal lengths. First, the focal lengths of the two negative lenses in lens group B (f_2 and f_4), which happen to be identical in our symmetric configuration, mainly determine the displacement magnification of the zoom. This point can be anticipated as the change in lens group B 's position implements the zoom. Specifically, the OCZ lens can achieve a wider span of working distances under zoom when L_2 and L_4 have larger refracting power, namely, smaller $|f_2|$ and $|f_4|$ values. Second, L_3 needs to have a refracting power that is similar in magnitude but opposite in sign compared to L_2 and L_4 so as to sufficiently compensate for the divergence introduced by lens group B . Finally, the symmetrically paired lenses L_1 and L_5 are chosen to have a refractive power

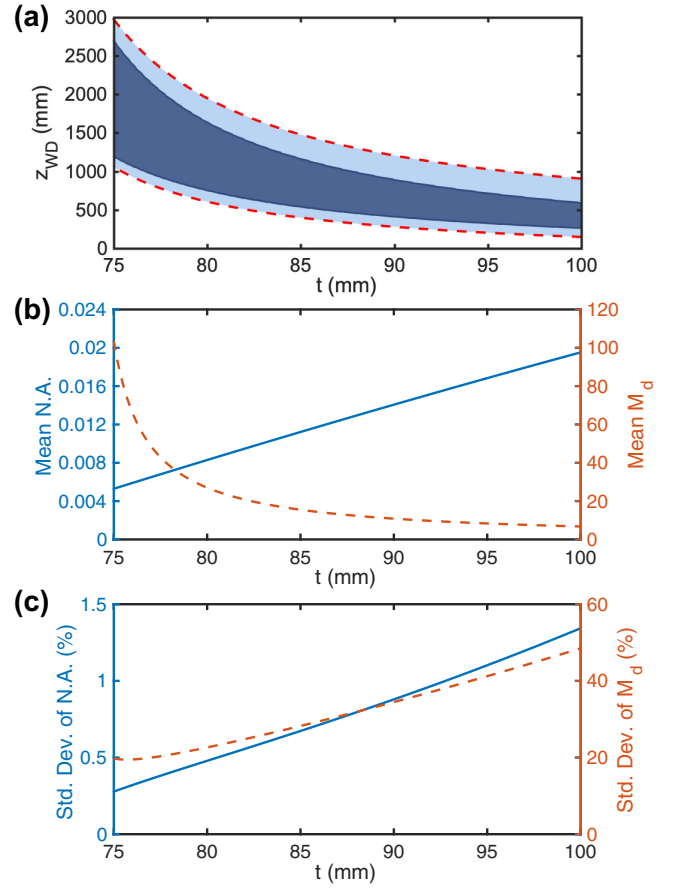


FIG. 3. Configuration of the OCZ lens via the intragroup lens spacing t for a desired range of z_{WD} under zoom. (a) The range of working distances the zoom covers for a given t with a peak-to-peak error of less than 1% for the NA (dark-blue region). The mechanical limit of the zoom when using 15-mm-thick lenses (red dashed lines). (b),(c) The mean and standard deviation of the numerical aperture (blue line) and the displacement magnification (red dashed line) across the zoom range as a function of t .

considerably smaller with respect to L_3 . This arrangement is intended for sending the focal point position far from the OCZ lens assuring a sufficient range for z_{WD} while zooming.

Once the focal lengths of the five lenses are decided we can select an intragroup lens spacing t which produces a desired range for z_{WD} under zoom. Figure 3(a) is a calculation of the range of working distances the zoom can cover for a given t . The intrinsic limits of the z_{WD} arise from mechanical restrictions due to the lenses coming into physical contact while having a nonzero thickness Δ . By setting a boundary of $\Delta < x < t - \Delta$ for the zoom we can obtain the limits for z_{WD} as the red dashed lines depicted in Fig. 3(a), where Δ was set to 15 mm. This boundary accurately reflects our experimental setup with the lenses enclosed in lens-holding mounts and taking into account an increased optical path length in the thick lenses. The dark-blue-shaded region indicates a preferable range of z_{WD} where the peak-to-peak change in the NA during zoom is under 1% of its center value. Even in the light-blue-shaded region where the NA changes a relatively large

amount compared to the dark-shaded region, the variation is kept below 8%, which is more than suitable for a typical ODT.

The range of z_{WD} achieved by the zoom is not the only parameter modified when changing t . The numerical aperture and displacement magnification under zooming motion are altered when t is adjusted for a targeted outcome. Figure 3(b) plots the mean values of the NA and the M_d as a function of t . The mean values are taken over the zoom position, such that the mean of a function f can be described as $\bar{f}(t) = \int_{\Delta}^{t-\Delta} f(x, t) dx / (t - 2\Delta)$. Recall that Fig. 2(a) corresponds to the case when $t = 86.4$ mm, where the change in NA and M_d while zooming can be explicitly seen. In order to quantify this change under zoom, we numerically calculate the standard deviations of the NA and the M_d as a function of t . The amount of variation exhibited by these parameters across the zoom boundary for a given t is plotted in Fig. 3(c).

According to the calculations in Fig. 3, as t decreases the range of z_{WD} under zoom increases along with the mean displacement magnification. Meanwhile, the minimum working distance that the OCZ lens can produce is increased, which can present a lower limit for t in actual experiments. One thing to note when decreasing t for the purpose of increasing the z_{WD} range under zoom is that the mean numerical aperture will also decrease. Nonetheless, this reduction of the NA can be made up for by expanding the input beam size for a desired NA value. We would like to stress that while the standard deviation of the numerical aperture under zoom is generally well suppressed by virtue of the compensating design of the zoom lens, it still increases with larger t in Fig. 3(c). The standard deviation of the displacement magnification also increases with t to values up to 50%. In spite of these relatively large changes in M_d while zooming, its adverse effects to the ODT motion can be readily compensated for via control over the linear stage actuating the zoom as mentioned above.

For experimental implementation, t can be optimized considering the following arguments. Ideally, t should be minimized in order to get wider ranges of the working distance, larger displacement magnifications, and smaller performance variations under zoom. However, in practice, not only is the input beam size limited due to finite lens diameters, but the optical access is severely constrained around the ultrahigh-vacuum system. Increasing lens alignment errors will also need to be considered. Hence realistic experimental conditions may advocate increasing t in order to gain larger NA values, decrease the minimum working distance, and attain better ODT position stability. Ultimately, for typical atom transport experiments, t should be minimized to within practical restrictions given by the experimental setup.

III. OPTICAL EVALUATION OF OCZ LENS PERFORMANCE

The experimental setup consists of five commercially available lenses. The 250-mm focal length L_1 and L_5 lenses are 2 in.-diameter achromatic doublets with antireflection coating for the visible wavelengths (Thorlabs AC508-250-A). The -80-mm focal length L_2 and L_4 lenses are 40-mm-diameter negative doublets with MgF₂ coating (Edmund Optics 63-764). The 80-mm focal length L_3 lens is a 40-mm-diameter achromatic doublet lens with MgF₂ coating (Edmund Optics

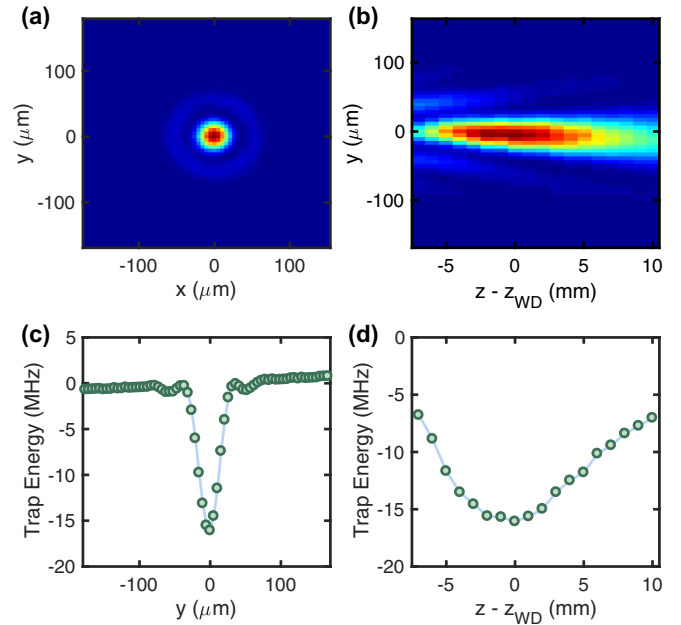


FIG. 4. Beam profile measurements of the propagating ODT beam. (a) Image of the transverse (x - y) plane at the focus position. (b) Constructed intensity profile of the beam propagating along the z direction (optical axis) through the focus position. (c) Calculated trap potential along the y direction (gravitational axis) using the beam profile from (a). (d) Calculated trap potential along the z direction using the beam profile from (b). All measurements and calculations correspond to $z_{\text{WD}} = 600$ mm.

45-105). The lenses L_2 and L_4 move along the optical axis by means of a linear motor stage (Newport XMS160) with a maximum travel range of 160 mm, minimum incremental motion of 1 nm, and position accuracy of $\pm 0.5 \mu\text{m}$.

In order to accurately assess the performance of the OCZ lens we take multiple images of the beam along the optical axis for various zoom positions. Analysis of these images enables direct evaluation of the focus position, beam radius, and axial intensity variations. Figures 4(a) and 4(b) show an example of this direct optical measurement for $t = 86.4$ mm and $z_{\text{WD}} = 600$ mm. The propagating beam is directly incident on a monochrome CCD (Thorlabs DCC 1545M) with $5.2 \mu\text{m} \times 5.2 \mu\text{m}$ pixels after being sufficiently attenuated with ND filters to profile the focusing beam. Figure 4(a) corresponds to the beam profile image at focus, $z = z_{\text{WD}}$, when we input a Gaussian beam into the OCZ lens of radius 6 mm. The y axis is along the direction opposite to gravity, and the x axis is orthogonal to the y and z axes. We observe a beam waist of $w_0 \approx 26.8 \mu\text{m}$. This measurement is $\sim 15\%$ larger than the diffraction-limited beam waist of $23.3 \mu\text{m}$ calculated for a 6-mm Gaussian beam input. In our experiment, spherical aberration from the OCZ lens and an astigmatic input beam are the main contributors to broadening the beam waist from its calculated value. Diffraction rings coming from the limited aperture size of L_3 can also be identified. Note that the input Gaussian beam radius in our experiment is 40% smaller than that calculated in the previous Sec. II A [refer to Fig. 1(b)], and this difference is taken into account by modifying the expected (NA) proportionally by a factor of 0.6. Parameters

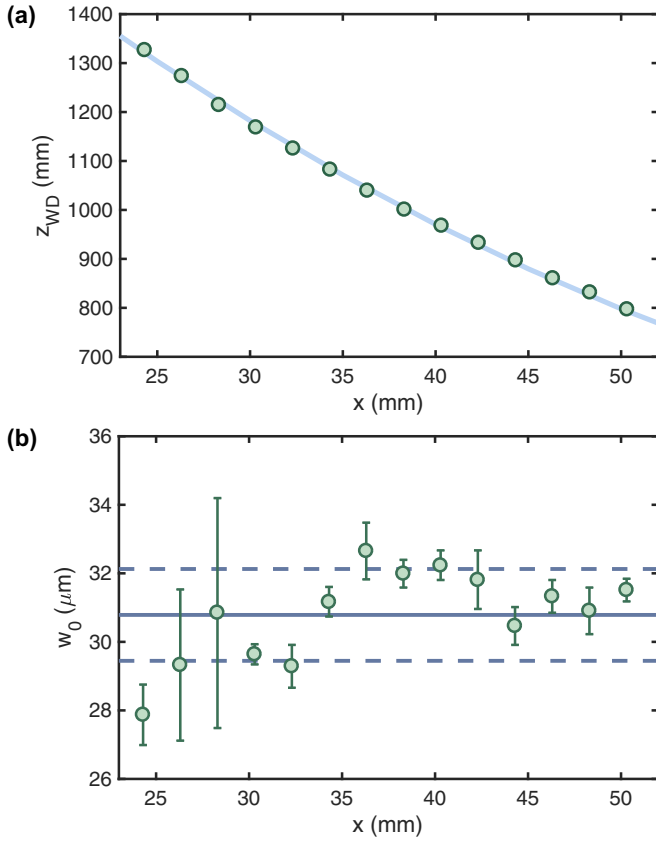


FIG. 5. Optically evaluated zoom performance of the OCZ lens. (a) The measured working distance as a function of zoom position (green circles) and the thin-lens model calculation fitted for the intragroup lens spacing resulting in $t = 86.4$ mm (blue line). (b) The measured beam waist radius as a function of zoom position (green circles). Indicators of the sample mean (solid line) and standard deviation (dashed line) of the measured beam waist.

such as working distance and longitudinal magnification are unchanged.

A set of images is acquired across different z positions in the vicinity of the focal point to obtain an intensity profile along z , e.g., Fig. 4(b). For the case in Fig. 4(b), the Rayleigh range is measured to be ~ 6 mm, which is $\sim 40\%$ larger than the expected value of $z_R = \pi w_0^2 / \lambda = 4.2$ mm. The discrepancy is mainly due to various aberrations affecting the beam wavefront, and the input beam profile deviating from a Gaussian. Figures 4(c) and 4(d) show the potential profile of our measured ODT for ^{174}Yb atoms in the 1S_0 ground state and includes gravitational acceleration along the $-y$ direction. The laser power used in the calculations is 20 W at wavelength 532 nm resulting in a trap depth of ~ 16 MHz.

In order to test the repeatability of the OCZ lens, we translate the ODT position by 600 mm back and forth 120 times and measure the beam profile after each round trip. No significant shift of the ODT position in the transverse x - y plane was measured, which we estimate to be at maximum $0.15 \mu\text{m}$ along both x and y directions. Measurements for the position along the axial (z direction) is severely limited due to the long Rayleigh length of the focusing beam. Specifications of the

linear stage suggest that we can estimate an axial position accuracy of approximately $\pm 10 \mu\text{m}$.

The beam focus profile was measured, as in Fig. 4, for multiple zoom positions used for transporting atoms in our experiment. Figure 5(a) shows the measured focus position, represented as z_{WD} , for a range of zoom positions from $x = 24.3$ mm up to $x = 50.3$ mm. Despite the fact that in practice we use thick achromatic lenses, the measured z_{WD} under zooming motion can be fit reliably to our calculations based on ideal thin lenses (blue line). Therefore, the fit result of $t = 86.4$ mm is actually an *effective* intragroup lens spacing. The actual spacing between the thick lenses is measured to be ~ 5 mm longer, which is in agreement with the estimated increase in optical path length of $\Delta \times (n - 1) / n \approx 5$ mm, where n is the index of refraction of the glass. The calculations shown in Figs. 1(b) and 2 are based on this fitted value of $t = 86.4$ mm for rigorous illustration of the experimental setup.

Figure 5(b) shows the measured beam waist for the same zoom positions as above. These w_0 measurements and their error bars (fit residuals) are extracted from compiled data of multiple beam profile images such as those shown in Fig. 4. Although the beam waist is generally broadened due to lens aberrations compared to its diffraction-limited value, it is consistently kept near its mean value of $30.8 \mu\text{m}$ [solid line in Fig. 5(b)] across the zoom range. The relatively well maintained beam waist experimentally confirms the compensating capability of the OCZ lens to keep the ODT profile constant. Furthermore, we can estimate that the depth of the ODT will marginally vary during transport with a standard deviation of less than 10%, which is sufficiently small for reliable atom transfer. Nonetheless, additional improvements regarding aberration control can be achieved by using custom lenses for the OCZ lens elements and high-power optical fibers for mode filtering of the incident beam.

IV. TRANSPORTING LASER-COOLED ^{174}Yb ATOMS WITH THE OCZ LENS

In this section, we report the performance of the OCZ lens when employed for transporting cold atoms by distances on the order of hundreds of millimeters. A cold atomic gas of ^{174}Yb is prepared with a core-shell magneto-optical trap (MOT) in an ultrahigh-vacuum system depicted in Fig. 6(a) [46]. The MOT is then compressed [47] for 100 ms to achieve a highly dense atomic sample of temperature $\sim 5 \mu\text{K}$. The ODT, which is aligned to the center of the atomic sample, is turned on during the MOT compression step with active power stabilization. After a fraction of the laser-cooled atoms are loaded into the ODT, the MOT is subsequently turned off and the atoms trapped in the ODT will be kept suspended against gravity while the untrapped atoms fall.

Figure 6(b) is an absorption image of the atoms taken along the axial direction of the ODT (z direction) 2 ms after releasing the atoms from the ODT and 20 ms after switching off the MOT. This image clearly shows the spatial separation between the atoms trapped in the ODT (encircled by red dotted line) positioned above a dispersing thermal cloud of untrapped atoms. Before initiating the transport, we hold the atoms in a stationary ODT for $\tau_0 = 500$ ms while unwanted

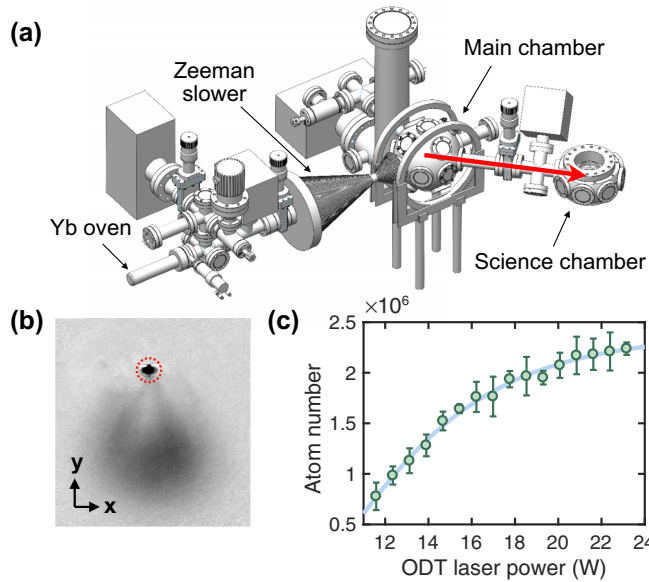


FIG. 6. (a) Schematic of the vacuum system for cooling and trapping Yb atoms. Atom transport by 600 mm is illustrated with red arrow. (b) Absorption image example taken along the z -axis after 2 ms time-of-flight. Atoms loaded into the ODT (encircled by red dotted line) can be seen above the falling untrapped atoms released from the MOT. (c) Number measurements of atoms trapped for 7.5 seconds in a stationary ODT as a function of the ODT laser power. The data is fitted to a cumulative energy distribution function taking into account Maxwell-Boltzmann statistics (blue line).

internal dynamics of the trapped atomic sample subside. Figure 6(c) is a measurement of the number of atoms trapped in a stationary ODT for various ODT laser powers. The time of measurement is set to 7.5 s after turning off the MOT, which serves as a reference for the atom transport measurements. The data points and errorbars correspond to the average and standard deviation of four independent measurements of the atom number via absorption image analysis. We fit the data with a scaled cumulative distribution function (CDF) for the energy assuming Maxwell-Boltzmann statistics. Defining $\epsilon \equiv E/k_B T$ where E is the energy, k_B is the Boltzmann constant, and T is the temperature, we can express the CDF as $\text{erf}(\sqrt{\epsilon}) - \frac{2}{\sqrt{\pi}}\sqrt{\epsilon}\exp(-\epsilon)$. The fit coefficients indicate that the minimum amount of laser power needed to have any trapped atoms remaining in the ODT is 8.5 W corresponding to a trap depth of $\sim 320 \mu\text{K}$.

Finally, we transport the ODT by 600 mm from the *main* chamber, where the atoms are initially cooled and trapped, into an adjacent *science* chamber. The transport path is depicted in Fig. 6(a) with a red arrow. The trapping conditions of the ODT during the transport is controlled with the ODT laser power and the acceleration of the zoom motion. Figure 7(a) describes the transport sequence by plotting the velocity of the ODT position with respect to time. As mentioned above, the laser-cooled atoms in the MOT are loaded into the ODT and held stationary for $\tau_0 = 500$ ms before transport. The acceleration of the moving ODT is controlled with the programmable linear stage where the absolute values of the acceleration and deceleration are identical and set to be constant valued. The

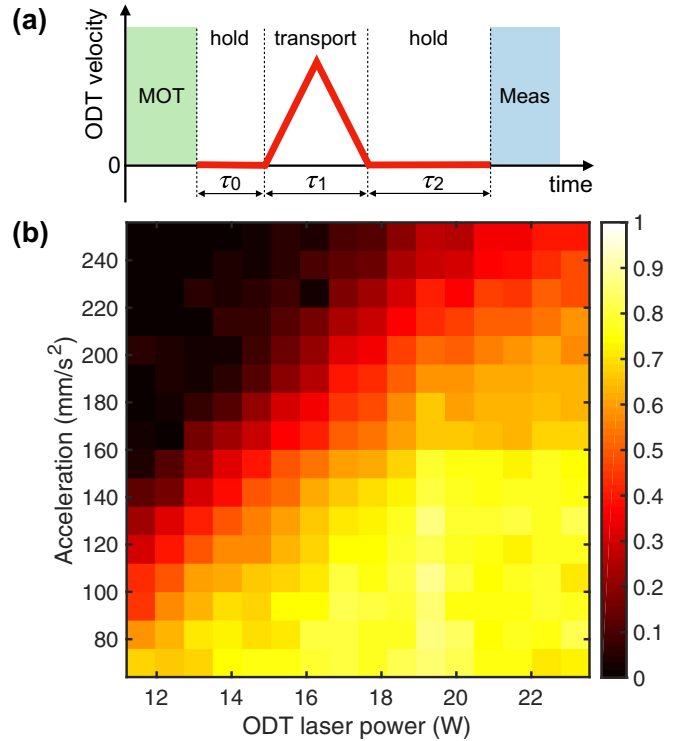


FIG. 7. (a) Schematic of the atom transport sequence in terms of the velocity of the ODT position. (b) Transport efficiency of atoms delivered to science chamber as a function of the ODT laser power and acceleration of the ODT position during transport.

velocity is never arbitrarily limited so as to be saturated during movement. Note that the time strictly required for traveling 600 mm (τ_1) depends on the acceleration of the transport. Since we fix the total time that the atoms are kept in the ODT before atom number measurements to be $\tau_0 + \tau_1 + \tau_2 = 7.5$ s, the atoms are held stationary for the remaining time τ_2 after transport.

In Fig. 7(b) we examine the efficiency of the transport by scanning two parameters: ODT laser power and transport acceleration. The transport efficiency is obtained by averaging the number of atoms that arrive at the science chamber for four independent experiments, and then normalizing with the no-transport measurement shown in Fig. 6(c). As per intuition, the atoms are more efficiently transported when the ODT laser power is high and the transport acceleration is low. The maximum transport efficiency is measured to be $\sim 89\%$ for which we can transport $\sim 2 \times 10^6$ atoms. Balancing transport time with atom number, we typically operate at a transport time of $\tau_1 = 3.6$ ss, corresponding to an ODT acceleration of 180 mm/s^2 , where we can transport $\sim 1.5 \times 10^6$ atoms with temperatures of $\sim 6 \mu\text{K}$ and atom cloud densities of $\sim 4 \times 10^{12}/\text{cm}^3$.

It is worth noting that in the frame of the moving ODT the trap shape is altered compared to a stationary ODT in a way that the trap depth along the axial direction decreases with increasing acceleration. Above a critical acceleration the axial trap depth is too shallow for atoms to be held in the trap for detection at the science chamber. Simple light shift calculations suggest that this critical acceleration should be proportional

to the ODT laser power. By fitting the data in Fig. 7(b) to the CDF for energy, we find the critical acceleration per laser power to be $30.4 \text{ mm}/(\text{s}^2\text{W})$, which is comparable to our estimated value of $39.2 \text{ mm}/(\text{s}^2\text{W})$ using light shift calculations. The discrepancy can be mainly attributed to effects from atom loss due to thermal redistribution.

V. CONCLUSION

In summary, we have explored the designing aspects and experimental implementation of an OCZ lens for cold atom transport. It was theoretically shown with the Gaussian beam propagation model and experimentally confirmed with optical beam profile measurements that the trap depth of the ODT is relatively well maintained during the transport. Using the ideal Gaussian beam calculations, we presented the transport range, variations of the numerical aperture, and displacement magnification of the moving ODT which were readily adjustable by tuning the lens spacings. Finally, we experimentally implemented an OCZ lens to our cold ^{174}Yb atom for transport by approximately 600 mm to an adjacent vacuum chamber. The atoms were transported with up to $\sim 89\%$ efficiency when compared to that without transport. This study displays the broad potential the OCZ lens has for use in various cold atom experiments which utilize moving ODTs for atom transport. Specifically, its compact form factor can decrease the overall length of the atom transfer setup by several times and in some cases an order of magnitude

compared to previous systems. Note that the OCZ lens can be further compressed from that experimentally demonstrated in this study for an even smaller form factor, but will require larger lenses for constant NA performances. Furthermore, the fact that the displacement magnification of the OCZ lens can be continuously tuned drastically enhances its versatility compared to conventional setups. As one example, multiple OCZ lenses can be precisely driven with a single translation stage in multichamber and multispecies experiments. Finally, the results of this research show that optical compensation, as opposed to mechanical compensation, can be a suitable method for zoom lens designs considering moving ODTs, particularly due to its high precision and repeatability. Future research regarding improved performance with respect to mitigating aberration, and achromatic designs for dual species ODTs are expected.

ACKNOWLEDGMENTS

This research was supported by the Institute of Information & Communications Technology Planning & Evaluation (IITP) grant funded by the Korea government (MSIT) (Grant No. 2019-0-01349), the National Research Foundation of Korea grant funded by the Korea government (MSIT) (Grant No. NRF-2019M3E4A1080398), and the R&D Convergence Program of NST (National Research Council of Science and Technology) of the Republic of Korea (Grant No. CAP-15-08-KRISS).

-
- [1] W. D. Phillips, Nobel lecture: Laser cooling and trapping of neutral atoms, *Rev. Mod. Phys.* **70**, 721 (1998).
 - [2] A. Urvoy, Z. Vendeiro, J. Ramette, A. Adiyatullin, and V. Vuletić, Direct Laser Cooling to Bose-Einstein Condensation in a Dipole Trap, *Phys. Rev. Lett.* **122**, 203202 (2019).
 - [3] I. Bloch, J. Dalibard, and W. Zwerger, Many-body physics with ultracold gases, *Rev. Mod. Phys.* **80**, 885 (2008).
 - [4] I. H. Deutsch and P. S. Jessen, Quantum-state control in optical lattices, *Phys. Rev. A* **57**, 1972 (1998).
 - [5] L.-M. Duan, E. Demler, and M. D. Lukin, Controlling Spin Exchange Interactions of Ultracold Atoms in Optical Lattices, *Phys. Rev. Lett.* **91**, 090402 (2003).
 - [6] H. Levine, A. Keesling, A. Omran, H. Bernien, S. Schwartz, A. S. Zibrov, M. Endres, M. Greiner, V. Vuletić, and M. D. Lukin, High-Fidelity Control and Entanglement of Rydberg-Atom Qubits, *Phys. Rev. Lett.* **121**, 123603 (2018).
 - [7] W. S. Bakr, J. I. Gillen, A. Peng, S. Fölling, and M. Greiner, A quantum gas microscope for detecting single atoms in a Hubbard-regime optical lattice, *Nature (London)* **462**, 74 (2009).
 - [8] C. Gross and I. Bloch, Quantum simulations with ultracold atoms in optical lattices, *Science* **357**, 995 (2017).
 - [9] R. Miller, T. E. Northup, K. M. Birnbaum, A. Boca, A. D. Boozer, and H. J. Kimble, Trapped atoms in cavity QED: Coupling quantized light and matter, *J. Phys. B: At., Mol. Opt. Phys.* **38**, S551 (2005).
 - [10] F. Brennecke, S. Ritter, T. Donner, and T. Esslinger, Cavity optomechanics with a Bose-Einstein condensate, *Science* **322**, 235 (2008).
 - [11] M. Takamoto, I. Ushijima, N. Ohmae, T. Yahagi, K. Kokado, H. Shinkai, and H. Katori, Test of general relativity by a pair of transportable optical lattice clocks, *Nat. Photonics* **14**, 411 (2020).
 - [12] S. Giovanazzi, A. Görlitz, and T. Pfau, Tuning the Dipolar Interaction in Quantum Gases, *Phys. Rev. Lett.* **89**, 130401 (2002).
 - [13] M. Tomza, K. Jachymski, R. Gerritsma, A. Negretti, T. Calarco, Z. Idziaszek, and P. S. Julienne, Cold hybrid ion-atom systems, *Rev. Mod. Phys.* **91**, 035001 (2019).
 - [14] D. E. Chang, J. S. Douglas, A. González-Tudela, C.-L. Hung, and H. J. Kimble, *Colloquium*: Quantum matter built from nanoscopic lattices of atoms and photons, *Rev. Mod. Phys.* **90**, 031002 (2018).
 - [15] A. Goban, C. L. Hung, S. P. Yu, J. D. Hood, J. A. Muniz, J. H. Lee, M. J. Martin, A. C. McClung, K. S. Choi, D. E. Chang, O. Painter, and H. J. Kimble, Atom-light interactions in photonic crystals, *Nat. Commun.* **5**, 3808 (2014).
 - [16] A. P. Hilton, C. Perrella, F. Benabid, B. M. Sparkes, A. N. Luiten, and P. S. Light, High-efficiency cold-atom transport into a waveguide trap, *Phys. Rev. Appl.* **10**, 044034 (2018).
 - [17] S. Okaba, T. Takano, F. Benabid, T. Bradley, L. Vincetti, Z. Maizelis, V. Yampol'skii, F. Nori, and H. Katori, Lamb-Dicke spectroscopy of atoms in a hollow-core photonic crystal fibre, *Nat. Commun.* **5**, 4096 (2014).
 - [18] A. Browaeys, H. Häffner, C. McKenzie, S. L. Rolston, K. Helmerson, and W. D. Phillips, Transport of atoms in a quantum conveyor belt, *Phys. Rev. A* **72**, 053605 (2005).
 - [19] S. Schmid, G. Thalhammer, K. Winkler, F. Lang, and J. H. Denschlag, Long distance transport of ultracold atoms using a 1D optical lattice, *New J. Phys.* **8**, 159 (2006).

- [20] H. Kim, W. Lee, H.-g. Lee, H. Jo, Y. Song, and J. Ahn, *In situ* single-atom array synthesis using dynamic holographic optical tweezers, *Nat. Commun.* **7**, 13317 (2016).
- [21] D. Stuart and A. Kuhn, Single-atom trapping and transport in DMD-controlled optical tweezers, *New J. Phys.* **20**, 023013 (2018).
- [22] M. Miranda, A. Nakamoto, Y. Okuyama, A. Noguchi, M. Ueda, and M. Kozuma, All-optical transport and compression of ytterbium atoms into the surface of a solid immersion lens, *Phys. Rev. A* **86**, 063615 (2012).
- [23] S.-Q. Shang, B. Sheehy, H. Metcalf, P. van der Straten, and G. Nienhuis, Velocity-Selective Resonances and Sub-Doppler Laser Cooling, *Phys. Rev. Lett.* **67**, 1094 (1991).
- [24] S. Händel, A. L. Marchant, T. P. Wiles, S. A. Hopkins, and S. L. Cornish, Magnetic transport apparatus for the production of ultracold atomic gases in the vicinity of a dielectric surface, *Rev. Sci. Instrum.* **83**, 013105 (2012).
- [25] K. Nakagawa, Y. Suzuki, M. Horikoshi, and J. B. Kim, Simple and efficient magnetic transport of cold atoms using moving coils for the production of Bose–Einstein condensation, *Appl. Phys. B* **81**, 791 (2005).
- [26] W. Hänsel, J. Reichel, P. Hommelhoff, and T. W. Hänsch, Magnetic Conveyor Belt for Transporting and Merging Trapped Atom Clouds, *Phys. Rev. Lett.* **86**, 608 (2001).
- [27] S. Minniberger, F. Diorico, S. Haslinger, C. Hufnagel, C. Novotny, N. Lippok, J. Majer, C. Koller, S. Schneider, and J. Schmiedmayer, Magnetic conveyor belt transport of ultracold atoms to a superconducting atomchip, *Appl. Phys. B* **116**, 1017 (2014).
- [28] M. Greiner, I. Bloch, T. W. Hänsch, and T. Esslinger, Magnetic transport of trapped cold atoms over a large distance, *Phys. Rev. A* **63**, 031401(R) (2001).
- [29] J. Reichel, W. Hänsel, and T. W. Hänsch, Atomic Micromanipulation with Magnetic Surface Traps, *Phys. Rev. Lett.* **83**, 3398 (1999).
- [30] T. L. Gustavson, A. P. Chikkatur, A. E. Leanhardt, A. Görlitz, S. Gupta, D. E. Pritchard, and W. Ketterle, Transport of Bose-Einstein Condensates with Optical Tweezers, *Phys. Rev. Lett.* **88**, 020401 (2001).
- [31] C. Gross, H. C. J. Gan, and K. Dieckmann, All-optical production and transport of a large ${}^6\text{Li}$ quantum gas in a crossed optical dipole trap, *Phys. Rev. A* **93**, 053424 (2016).
- [32] F. Finger, A transport laser with shape and amplitude control for ultracold strontium atoms, Master thesis, Technical University of Munich, 2018.
- [33] Y. Miroshnychenko, An atom-sorting machine, Ph.D. thesis, University of Bonn, 2006.
- [34] A. Ashkin, J. M. Dziedzic, J. E. Bjorkholm, and S. Chu, Observation of a single-beam gradient force optical trap for dielectric particles, *Opt. Lett.* **11**, 288 (1986).
- [35] J. Enger, M. Goksör, K. Ramser, P. Hagberg, and D. Hanstorp, Optical tweezers applied to a microfluidic system, *Lab Chip* **4**, 196 (2004).
- [36] A. N. Grigorenko, N. W. Roberts, M. R. Dickinson, and Y. Zhang, Nanometric optical tweezers based on nanostructured substrates, *Nat. Photonics* **2**, 365 (2008).
- [37] J. Lee, S.-Y. Teh, A. Lee, H. H. Kim, C. Lee, and K. K. Shung, Single beam acoustic trapping, *Appl. Phys. Lett.* **95**, 073701 (2009).
- [38] A. Ashkin and J. Dziedzic, Optical trapping and manipulation of viruses and bacteria, *Science* **235**, 1517 (1987).
- [39] Y.-F. Chen, X. Serey, R. Sarkar, P. Chen, and D. Erickson, Controlled photonic manipulation of proteins and other nanomaterials, *Nano Lett.* **12**, 1633 (2012).
- [40] R. Grimm, M. Weidemüller, and Y. B. Ovchinnikov, Optical dipole traps for neutral atoms, *Adv. At., Mol., Opt. Phys.* **42**, 95 (2000).
- [41] E. W. Streed, A. P. Chikkatur, T. L. Gustavson, M. Boyd, Y. Torii, D. Schneble, G. K. Campbell, D. E. Pritchard, and W. Ketterle, Large atom number Bose-Einstein condensate machines, *Rev. Sci. Instrum.* **77**, 023106 (2006).
- [42] J. Léonard, M. Lee, A. Morales, T. M. Karg, T. Esslinger, and T. Donner, Optical transport and manipulation of an ultracold atomic cloud using focus-tunable lenses, *New J. Phys.* **16**, 093028 (2014).
- [43] G. Wooters and E. W. Silvertooth, Optically compensated zoom lens, *J. Opt. Soc. Am.* **55**, 347 (1965).
- [44] G. H. Matter and E. T. Luszcz, A family of optically compensated zoom lenses, *Appl. Opt.* **9**, 844 (1970).
- [45] S. Pal and L. N. Hazra, Structural design of four-component optically compensated zoom lenses: Use of evolutionary programming, *Optik* **123**, 1534 (2012).
- [46] J. Lee, J. H. Lee, J. Noh, and J. Mun, Core-shell magneto-optical trap for alkaline-earth-metal-like atoms, *Phys. Rev. A* **91**, 053405 (2015).
- [47] S. Dörscher, A. Thobe, B. Hundt, A. Kochanke, R. Le Targat, P. Windpassinger, C. Becker, and K. Sengstock, Creation of quantum-degenerate gases of ytterbium in a compact 2D-/3D-magneto-optical trap setup, *Rev. Sci. Instrum.* **84**, 043109 (2013).